Visualizing Shape Deformations with Variation of Geometric Spectrum

Jiaxi Hu, Hajar Hamidian, Zichun Zhong, and Jing Hua

Abstract—This paper presents a novel approach based on spectral geometry to quantify and visualize non-isometric deformations of 3D surfaces by mapping two manifolds. The proposed method can determine multi-scale, non-isometric deformations through the variation of Laplace-Beltrami spectrum of two shapes. Given two triangle meshes, the spectra can be varied from one to another with a scale function defined on each vertex. The variation is expressed as a linear interpolation of eigenvalues of the two shapes. In each iteration step, a quadratic programming problem is constructed, based on our derived spectrum variation theorem and smoothness energy constraint, to compute the spectrum variation. The derivation of the scale function is the solution of such a problem. Therefore, the final scale function can be solved by integral of the derivation from each step, which, in turn, quantitatively describes non-isometric deformations between two shapes. To evaluate the method, we conduct extensive experiments on synthetic and real data. We employ real epilepsy patient imaging data to quantify the shape variation between the left and right hippocampi in epileptic brains. In addition, we use longitudinal Alzheimer data to compare the shape deformation of diseased and healthy hippocampus. In order to show the accuracy and effectiveness of the proposed method, we also compare it with spatial registration-based methods, e.g., non-rigid Iterative Closest Point (ICP) and voxel-based method. These experiments demonstrate the advantages of our method.

Index Terms—Geometry-based Technique, Spectral Analysis, Biomedical Visualization

1 Introduction

Morphometric analysis of 3D surface objects are very important in many biomedical applications and clinical diagnoses. Its critical step lies in shape comparison. Many different kinds of shape analyses were presented in the literature [20, 21, 39, 6] for shape representation and comparison. The spatial geometric properties of surface shapes, such as curvature, geodesic distance, etc., were used to represent and differentiate various shapes [7, 20]. There also exist more advanced methods for representing and differentiating shapes. For example, shape distribution method defines shape properties based on distance, angle, area and volume measurements between random surface points [21]. Then, the similarity between two objects can be determined by a pseudo-metric which is calculated with distances between the distributions. Geometry hashing method [39] represents a shape with some local interest features, such as points, lines, and so on, which can then be used for computing the shape difference. Graph-based method analyzes a 3D surface object by transforming it to a graph and converts the shape comparison into a graph problem [5, 6]. Note that the aforementioned shape analysis and comparison methods are challenged by irregular mesh samplings and complex/subtle deformations between shapes.

Shape spectrum, inspired by Fourier transform in signal processing [27], is another method to represent and differentiate shapes. This method was applied on graphs earlier. Considering a discrete meshes as a graph, shape spectrum is defined by a Laplacian matrix of the vertices and their connections. Using the concept of Fourier transform, the eigenvalues of the Laplacian matrix define the spectrum of the graph, and the eigenfunctions are the orthogonal bases. Therefore, the functions defined on graphs can be projected to the orthogonal bases and analysed in the spectrum domain. Karni and Gotsman [14] used this projection for smoothing and mesh comparison purposes. Jain and Zhang [12] employed the extended version of this method for shape registration in the spectrum domain. However, the Laplace spectrum approach focuses more on the connectivity of the graph which may lead to distorted mappings [42]. Along this direction, Reuter [27] and Lévy [17] defined a shape spectrum approach with the Laplace-Beltrami operator on a manifold and employed the eigenvalues and eigenfunctions as a global shape descriptor [26, 28, 25]. Using the eigenvalues and eigenfunctions, Rustamov proposed a modified shape distribution method in [31]. As the geometry changes, the spectrum will change as well. Therefore, the similarity and difference among shapes can be described using this method. However, through the direct use of the decomposed eigenvalues and eigenfunctions, these spectral methods can only describe the global difference between shapes. They are neither able to localize the shape difference nor can they quantify non-isometric deformations.

In this paper, we focus on spectrum alignment of general shapes using the eigenvalue variation in order to quantify the non-isometric deformations between surface shapes. In our approach, shapes are automatically aligned by calculating the metric scaling on both shapes. Our method defines the surface shape deformation by the variation of Laplace-Beltrami spectrum of the shapes and quantifies the multi-scale deformations through the use of different sets of eigenvalues. Compared to the traditional approaches, it can detect and localize small non-isometric deformations in addition to global difference of the shapes, without using any defined landmarks on the manifolds. This is because the spectrum only depends on the intrinsic geometry of the shape and is invariant to spatial translation, rotation, scaling and isometric deformation. This method is computationally affordable and suitable to map surface shapes for non-isometric deformation analysis.

1.1 Related Works

In general, there are two categories of methods for detection and categorization of 3D shape deformation: spatial registration methods and spectral methods. Spatial registration methods usually require well-defined features or landmarks to map two shapes [44, 36]. It becomes even more challenging when the landmarks are difficult to define in certain 3D shapes, such as hippocampus, heart, etc. Iterative Closest Point (ICP) method introduced by Besl and Mckay in [1] is one of the popular approaches in spatial registration-based methods. In this approach, the initial transformation for global matching is first estimated and then the closest points are found by minimizing the distance between two shapes. In spite of the simplicity of the algorithm, it is computationally costly to identify the closest points and it does not converge very fast. The ICP method has been used in many research areas such as multi-modality image registration [35]. They tried to

• *Jiaxi Hu, Hajar Hamidan, Zichun Zhong, and Jing Hua are with Wayne State University. Email: {jiaxihu—nasim.hamidian—zichunzhong—jinghua}@wayne.edu.*
• *Correspondence to Jing Hua.*

Manuscript received 31 Mar. 2016; accepted 1 Aug. 2016. Date of publication 15 Aug. 2016; date of current version 23 Oct. 2016.
For information on obtaining reprints of this article, please send e-mail to: reprints@ieee.org, and reference the Digital Object Identifier below.
Digital Object Identifier no. 10.1109/TVCG.2016.2598790

find the most-likely correspondence between two shapes using principal direction tree search. Han et al. [8] enhanced the ICP method for registering the large-scale 3D environment models. They tried to avoid the local minima to reach an optimal registration. According to their experiments, the computational time is around 20 times more than standard ICP. There are many other spatial registration methods that can be applied on 3D shapes for medical applications, such as Flirt [13] and surface parameterization-based approaches [43]. These methods use atlases and landmarks as well.

Spectral methods, on the other hand, do not need any landmarks. By definition, shape spectrum represents the information of intrinsic local geometry. It is invariant to isometric deformations and different triangulations. Also, the computing time is affordable and it can reveal the fine characteristics of the shape. Because of these important advantages of Laplace-Beltrami spectrum, this method is used by lots of studies and many shape analysis approaches such as shape recognition and shape matching [24]. However, these spectral methods can only describe the global difference between shapes by directly using the decomposed eigenvalues and eigenfunctions. Reuter et al. in [26] discussed that spectrum is invariant to small amount of noise but high level noise or small non-isometic deformation can change the spectrum dramatically. The change of shape spectrum is less studied in the literature. In reality, many deformations, such as heart motion, brain surface development, and so on, break isometry. Hence, applying geometric spectrum methods for analyzing non-isometric deformations is very challenging. Recent approaches [33, 34] showed the shape spectrum can be controlled with a scale function on the Riemann metric. Shi et al. discussed in [33] that the eigenvalues and eigenfunctions change according to the Riemann metric of the manifold. Since their work focused on generating a dense registration, the eigenvalue variation was not studied. In [34], Shi et al. used difference between the eigenfunctions of two surfaces to generate a conformal map directly between them. To this end, they minimize the difference between surfaces in the Laplace-Beltrami embedding space using optimization approaches. This study focused on eigenfunction variation and the method was time costly. For instance, for mapping two hippocampal surfaces with 1000 vertices, the procedure took around 20 minutes. Recently, Li et al. [18] proposed generalized local-to-global features on 3D geometric models, coupled with both local (differential) and global (integral) geometric attributes, based on spectral graph wavelets. There are recent advances in the field of spectral shape analysis closely related to the proposed approach. For instance, Kovnatsky et al. [16] showed how to modify (align) the eigenfunctions of the Laplace-Beltrami operator in order to match non-isometric shapes. Rodolà et al. [29] applied a Laplacian perturbation analysis (variation of eigenvalues and eigenfunctions), in order to show spectral properties of near-isometric manifolds. Ovsjanikov et al. [23] proposed a spectral method for shape matching which is based on finding an alignment between eigenfunctions based on a set of linear constraints. Then, Ovsjanikov et al. [22] presented a method for finding functional correspondence between manifolds based on the geometric matrix completion framework [15]. In [22, 32, 41], visualizing shape deformations based on a spectral representation of the correspondence was shown. However, the key difference between the methods mentioned above and our proposed approach lies in the fact that our method is correspondence-free, i.e., a map between the two objects is not required in order to align the Laplacian spectra.

There are some other methods, besides the spectral and ICP-like approaches. One of these approaches is diffeomorphism, which usually yields global optima. For example, Windheuser et al. [38] proposed a framework for computing an elastic orientation-preserving matching of non-rigid 3D shapes. Some other approaches are based on minimizing metric distortion, such as [2, 30]. There also exists some recent works [3, 9, 10] for visualization of shape deformations.

This paper presents a new method for quantifying and visualizing the deformations between surface shapes through the variation of geometric spectrum. Given two triangle meshes, the spectra can be varied from one to another with a scale function defined on each vertex. The variation is expressed as a linear interpolation of eigenvalues of the two shapes. In each iteration step, a quadratic programming problem is constructed based on our derived spectrum variation theorem and smoothness energy constraint to compute the spectrum variation. The derivation of the scale function is the solution of such a problem. Therefore, the final scale function can be solved by integral of the derivation from each step, which, in turn, quantitatively describes non-isometric deformations between the two shapes. Our major contributions in this work can be summarized as follows:

- **We prove a theorem that the shape spectrum is a piecewise analytic to a scale function defined on the Riemann metric of the manifold.** Our theorem holds in both continuous domains and discrete triangle meshes and supports the variation of eigenvalues for non-isometrically deformed shapes. Therefore, it enables a quantitative method for deformation analysis.

- **We present a spectrum alignment algorithm for triangle meshes, supporting non-isometric deformation analysis.** In the discrete domain, the variation of eigenvalues in terms of the scale vector can be turned into a matrix form, which introduces a linear system. Together with the smoothness and local bound constraints, the linear system can be solved efficiently. After the eigenvalues are matched, the eigenfunction distributions are aligned as well. This means the shape spectrum can be controlled analytically through a scale vector, hence, non-isometric analysis is available within shape spectra.

- **Our developed system verifies the spectrum variation theorem and demonstrates the accuracy and efficiency of the spectral variation algorithm on visualization of non-isometrically deformed shapes.** The applications to biomedical imaging problems show that it is a viable solution for morphometric analysis and visualization in biomedical applications and clinical diagnoses.

2 Variation of the Eigenvalues and Eigenfunctions

In this work, we use Laplace-Beltrami operator to compute the geometric spectrum of a manifold. Let $f_1 \in C^2$ be a real function defined on a Riemannian manifold M. The Laplace-Beltrami operator $\triangle$ is defined as: $\triangle f_1 = \nabla \cdot (\nabla f_1)$, where ∇f_1 is the gradient of f_1 and $\nabla\cdot$ is the divergence on the Manifold M. We compute the eigenvalue of the Laplacian equation defined as follows:

$$\triangle f = -\lambda f, \tag{1}$$

where the family solution $\{\lambda_i\}$ is a real nonnegative scalar and will result in the corresponding real family functions of $\{f_i\}$ for $i = 0, 1, 2, ...$ To solve the differential equations, different methods can be employed such as finite element method (FEM) and discrete differential operator. In [27], Reuter et al. discretized the manifold and the Laplace-Beltrami operator by using FEM. In this paper, we use discrete differential operator to solve this problem. In this framework, a 2D manifold is discretized to triangle meshes of $M = (V, E, F)$, where V is the set of vertices, E is the set of edges and F is the set of faces. Assuming the neighborhood of a vertex is approximated with the area of its Voronoi region, a discrete Laplace-Beltrami operator can be defined with the average value over the area of the Voronoi region. Using this concept, the Laplacian-Beltrami matrix for the vertices of a triangle mesh can be constructed as

$$L_{ij} = \begin{cases} -\frac{\cot\alpha_{ij}+\cot\beta_{ij}}{2A_i} & \text{if } i,j \text{ are adjacent,} \\ \sum_k \frac{\cot\alpha_{ik}+\cot\beta_{ik}}{2A_i} & \text{if } i = j, \\ 0 & \text{otherwise,} \end{cases} \tag{2}$$

where α_{ij} and β_{ij} are the two angles opposite to the edge in the two triangles sharing the edges i, j and A_i is the area of Voronoi region at vertex i. k is the index of triangles within 1-ring neighborhood of the vertex i.

Therefore, Equation 1 turns to:

$$\mathbf{L}\mathbf{v} = \lambda\mathbf{v}, \tag{3}$$

where $\mathbf{v}$ is n dimensional vector for each λ and represents the function value at each vertex on the mesh. This equation is a generalized eigenvalue problem and is solved numerically by constructing a sparse matrix $\mathbf{W}$ and a diagonal matrix $\mathbf{S}$ such that:

$$W_{ij} = \begin{cases} -\frac{\cot\alpha_{ij}+\cot\beta_{ij}}{2} & \text{if } i,j \text{ are adjacent,} \\ \sum_k \frac{\cot\alpha_{ik}+\cot\beta_{ik}}{2} & \text{if } i = j, \\ 0 & \text{otherwise,} \end{cases}$$

and $S_{ii} = A_i$. Thus, the Laplace Matrix $\mathbf{L}$ is decomposed as $\mathbf{L} = \mathbf{S}^{-1}\mathbf{W}$ and the generalized eigenvalue problem can be presented as:

$$\mathbf{W}\mathbf{v} = \lambda\mathbf{S}\mathbf{v}. \tag{4}$$

As a result of non-isometric deformation, the eigenvalues and eigenfunctions of the shape dramatically change. On a compact closed manifold M with Riemann metric g, we define shape deformation as a time variant positive scale function $\omega(t) : M \rightarrow R^+$ such that $g^{\omega}_{ij} = \omega g_{ij}$ and $d\sigma^{\omega} = \omega d\sigma$, where $\omega(t)$ is nonnegative and continuously differentiable. By definition, the weighted Laplace-Beltrami operator becomes $\Delta^{g^{\omega}} = \frac{1}{\omega}\Delta^{g}$. Consider the ith solution of the weighted eigen problem, this equation can be written as:

$$\Delta^{g^{\omega}} f_i = -\lambda_i f_i, \tag{5}$$

or rewritten as

$$\Delta^{g} f_i = -\lambda_i \omega f_i, \tag{6}$$

where the eigenfunction f_i is normalized as

$$\int_M f_i^2 d\sigma^{\omega} = 1 \textbf{ for } i = 0, 1, 2, \ldots, \tag{7}$$

and orthogonal to other eigenfunctions, such that:

$$\int_M f_i f_j d\sigma^{\omega} = 0, j \neq i. \tag{8}$$

Next, we will explain and prove two theorems that guarantee the existence of a scale function which aligns shapes with non-isometric deformations.

Theorem 1. *$\lambda_i(t)$ is piecewise analytic and, at any regular point, the t-derivative of $\lambda_i(t)$ is given by:*

$$\dot{\lambda_i} = -\lambda_i \int_M \dot{\omega} {f_i}^2 d\sigma. \tag{9}$$

Proof of this theorem is provided in Appendix A. This theorem can be applied to discrete matrix as well. Assume that $\mathbf{\Omega}$ is a nonnegative, continuously differentiable and diagonal matrix, based on Equation 4, a weighted generalized eigenvalue problem can be presented as follows:

$$\mathbf{W}\mathbf{v}_i = \lambda_i \mathbf{\Omega}\mathbf{S}\mathbf{v}_i, \tag{10}$$

where λ_i and $\mathbf{v}_i$ are ith corresponding solution. The eigenvectors can be normalized as

$$< \mathbf{v}_i, \mathbf{v}_i >_{\mathbf{\Omega S}} = 1 \textbf{ for } i = 0, 1, 2, \ldots, \tag{11}$$

and orthogonal to each other, i.e.,

$$< \mathbf{v}_i, \mathbf{v}_j >_{\mathbf{\Omega S}} = 0, \textbf{ when } i \neq j. \tag{12}$$

Theorem 2. *λ_i is piecewise analytic and, at any regular point, the t-derivative of λ_i is given by:*

$$\dot{\lambda_i} = -\lambda_i {\mathbf{v}_i}^T \dot{\mathbf{\Omega}}\mathbf{S}\mathbf{v}_i, \tag{13}$$

Proof of this theorem is provided in Appendix B. Our theorems show that the spectrum is smooth and analytical to non-isometric local scale deformation. They support the variation of eigenvalues for the alignment of non-isometrically deformed shapes, hence an automatic registration-free method for deformation analysis.

3 Algorithm for Computing Spectral Variations

Based on the theorems proved in Section 2, this section will detail a discrete algorithm for the alignment of non-isometrically deformed shapes through the variation of eigenvalues. Consider two closed manifolds, M and N, represented with discrete triangle meshes, their first k_1 nonzero eigenvalues and eigenvectors are

$$\lambda_{M_i}, \mathbf{v}_{M_i}, \lambda_{N_i}, \text{ and } \mathbf{v}_{N_i}, \text{ for } i = 1, 2, \ldots, k_1.$$

To align two shapes we use first k_1 smallest eigenvalues. By increasing k_1, some high frequency deformations may be detected. As we mentioned before, the deformation is not isometric, thus the first k_1 eigenvalues of two manifolds are not the same. In order to align the first k_1 eigenvalues of N to those of M, a continuous scale diagonal matrix $\mathbf{\Omega}(\mathbf{t})$ is applied on N. $\mathbf{\Omega}$ is an n by n matrix, where n is the number of vertices on N. The element Ω_{ii} at the diagonal is a scale factor defined on each vertex on N. According to Theorem 2, the derivative of each eigenvalue is expressed by those of Ω_{ii} analytically. Thus, the scale matrix $\mathbf{\Omega}$ will introduce a variation and alignment from N to M on eigenvalues. The following will explain the details how to calculate the diagonal matrix $\mathbf{\Omega}$ numerically.

3.1 Matrix Eigenvalue Variation

We assume that the eigenvalues of N vary linearly towards those of M. This linear interpolation is represented as:

$$\lambda_i(t) = (1-t)\lambda_{N_i} + t\lambda_{M_i}, t \in [0, 1]. \tag{14}$$

At the beginning, $t = 0$, and $\lambda_i(0)$ starts as λ_{N_i}, while t reaches 1, $\lambda_i(1)$ aligned to λ_{M_i}. At any regular time $t \in [0, 1]$, the derivative is constant value and can be calculated as:

$$\dot{\lambda_i}(t) = \lambda_{M_i} - \lambda_{N_i}, t \in [0, 1]. \tag{15}$$

Combining Equations 15 and 13, the derivative of each $\lambda_i(t)$ leads to an equation of $\mathbf{\Omega}$ as follows:

$$-\lambda_i(t){\mathbf{v}_i(t)}^T \dot{\mathbf{\Omega}}\mathbf{S}\mathbf{v}_i(t) = \lambda_{M_i} - \lambda_{N_i}, t \in [0, 1]. \tag{16}$$

Each diagonal element Ω_{ii} represents a scale factor at vertex i on manifold N. $\mathbf{\Omega}(\mathbf{0})$ is an identity matrix on N, and $\mathbf{\Omega}(\mathbf{1})$ aligns the first k_1 nonzero eigenvalues of N to those of M. Although the time derivative of $\mathbf{\Omega}$ can be calculated in Equation 15 but solving this equation is not straightforward. We need to transform the individual integration equation into a linear system. We achieve this by extracting the diagonals as vectors $\mathbf{v}_{\mathbf{\Omega}}$ and $\mathbf{v}_{\mathbf{S}}$ and then employing Hadamard product, which is an element wise matrix product as follows:

$$\mathbf{A} \circ \mathbf{B} = \mathbf{C} \text{ such that } A_{ij} \cdot B_{ij} = C_{ij}. \tag{17}$$

Then, Equation 13 can be rewritten in a linear form as follows:

$$(\mathbf{v}_{\mathbf{S}} \circ \mathbf{v}_i \circ \mathbf{v}_i)^T \cdot \mathbf{v}_{\dot{\mathbf{\Omega}}} = \frac{\lambda_{N_i} - \lambda_{M_i}}{\lambda_i(t)}, t \in [0, 1]. \tag{18}$$

Note that, as the first k_1 eigenvalues are going to be aligned, we can get k_1 independent equations, which lead to a linear system as follows:

$$\mathbf{A} \cdot \mathbf{v}_{\dot{\mathbf{\Omega}}} = \mathbf{b}, \tag{19}$$

where $\mathbf{A}$ is a row stack of $(\mathbf{v}_{\mathbf{S}} \circ \mathbf{v}_i \circ \mathbf{v}_i)^T$ with k_1 rows and $\mathbf{b}$ is the right side of Equation 18.

Considering that practically k_1 is much less than the number of nodes in the mesh, the system is underdetermined and has no unique solution. Thus, suitable constrains are necessary to provide an optimized solution for the linear system.

3.2 Smoothness Constraints

In this work, we focus on the global smoothness of the scale factors distributed on N. Consider a scalar function $f \in C^2$ is define on the continuous manifold $< N_c, g >$. The gradient of f describes the local change of f. A smoothness energy of f is defined with the total squared magnitude of the gradient ∇f on N_c as:

$$E = \int_{N_c} \|\nabla f\|^2 d\sigma. \tag{20}$$

Note that ∇f is a vector, and the squared magnitude is calculated as a dot product:

$$\|\nabla f\|^2 = \nabla f \cdot \nabla f. \tag{21}$$

Then, the integral on N_c becomes

$$E = -\int_{N_c} f \Delta^g f d\sigma. \tag{22}$$

At time t, we investigate the scale function $\omega(t)$ and $d\omega|_t$. Then, we can obtain the following smoothness energy:

$$\begin{aligned} E &= -\int_{N_c} (\omega + d\omega)\Delta^g(\omega + d\omega)d\sigma \\ &= -\int_{N_c} d\omega\Delta^g d\omega d\sigma - 2\int_{N_c} \omega\Delta^g d\omega d\sigma - \int_{N_c} \omega\Delta^g\omega d\sigma. \end{aligned} \tag{23}$$

On the discrete triangle mesh N, the scale function is a vector $\mathbf{v}_{\mathbf{\Omega}}$, which is the diagonal of matrix $\mathbf{\Omega}$. The integral is a matrix product as follows:

$$\begin{aligned} \mathbf{E} &= < \mathbf{v}_{\mathbf{\Omega}} + \mathbf{v}_{\dot{\mathbf{\Omega}}}, \mathbf{L} \cdot (\mathbf{v}_{\mathbf{\Omega}} + \mathbf{v}_{\dot{\mathbf{\Omega}}}) >_{\mathbf{S}} \\ &= (\mathbf{v}_{\mathbf{\Omega}} + \mathbf{v}_{\dot{\mathbf{\Omega}}})^T \cdot \mathbf{S} \cdot \mathbf{L} \cdot (\mathbf{v}_{\mathbf{\Omega}} + \mathbf{v}_{\dot{\mathbf{\Omega}}}) \\ &= (\mathbf{v}_{\mathbf{\Omega}} + \mathbf{v}_{\dot{\mathbf{\Omega}}})^T \cdot \mathbf{W} \cdot (\mathbf{v}_{\mathbf{\Omega}} + \mathbf{v}_{\dot{\mathbf{\Omega}}}) \\ &= \mathbf{v}_{\dot{\mathbf{\Omega}}}^T \cdot \mathbf{W} \cdot \mathbf{v}_{\dot{\mathbf{\Omega}}} + 2\mathbf{v}_{\mathbf{\Omega}}^T \cdot \mathbf{W} \cdot \mathbf{v}_{\dot{\mathbf{\Omega}}} + \mathbf{v}_{\mathbf{\Omega}}^T \cdot \mathbf{W} \cdot \mathbf{v}_{\mathbf{\Omega}}. \end{aligned} \tag{24}$$

Assume that $\mathbf{v}_{\mathbf{\Omega}}$ is known at each time t and $\mathbf{v}_{\dot{\mathbf{\Omega}}}$ is to be solved in Equation 19. $\mathbf{v}_{\dot{\mathbf{\Omega}}}$ is going to minimize the quadratic smooth energy E_q at any time,

$$\mathbf{E}_q = \mathbf{v}_{\dot{\mathbf{\Omega}}}^T \cdot \mathbf{W} \cdot \mathbf{v}_{\dot{\mathbf{\Omega}}} + 2\mathbf{c}^T \cdot \mathbf{v}_{\dot{\mathbf{\Omega}}}, \tag{25}$$

where $\mathbf{c} = \mathbf{W} \cdot \mathbf{v}_{\mathbf{\Omega}}$. In order to preserve the physical availability, $\mathbf{v}_{\mathbf{\Omega}}$ must be bounded, i.e., the scale factor cannot be zero or negative; and it cannot be infinite either. We denote a lower bound and an upper bound with $\mathbf{h}_l, \mathbf{h}_u > \mathbf{0}$, where $\mathbf{h}_l$ and $\mathbf{h}_u$ are n dimensional constant vector. $\mathbf{v}_{\dot{\mathbf{\Omega}}}$ must satisfy

$$\mathbf{h}_l \leq \mathbf{v}_{\mathbf{\Omega}} + \mathbf{v}_{\dot{\mathbf{\Omega}}} \leq \mathbf{h}_u. \tag{26}$$

This inequality bound can be written into a matrix form:

$$\mathbf{G} \cdot \mathbf{v}_{\dot{\mathbf{\Omega}}} \leq \mathbf{h}, \tag{27}$$

where $\mathbf{G}$ is stack of identity matrices as

$$\mathbf{G}_{2n\times n} = \begin{pmatrix} -\mathbf{I}_{n\times n} \\ \mathbf{I}_{n\times n} \end{pmatrix}, \tag{28}$$

and $\mathbf{h}$ is a $2n$ dimensional vector as

$$\mathbf{h}_{2n\times 1} = \begin{pmatrix} \mathbf{v}_{\mathbf{\Omega}} - \mathbf{h}_l \\ \mathbf{h}_u - \mathbf{v}_{\mathbf{\Omega}} \end{pmatrix}. \tag{29}$$

The linear system (Equation 19), smoothness constraint (Equation 25), and constant bound (Equation 27) introduce a quadratic programming problem at each time t. Assume the eigenvalues and eigenvectors are known at each time t, the derivative of the scale matrix $\dot{\mathbf{\Omega}}$ is the solution of such quadratic programming.

3.3 Linear Integration

In Section 3.2, we have shown that at each time t, the derivative of the scale function can be calculated as a solution of a quadratic programming. In the initial state, the scale function is identity which starts from manifold N itself. The final scale matrix can be achieved by the following integral:

$$\mathbf{\Omega}(\mathbf{1}) = \mathbf{I} + \int_0^1 \dot{\mathbf{\Omega}} dt. \tag{30}$$

This equation aligns the first k_1 nonzero eigenvalues from N to M. This integration is discretely approximated with an iteration. We divide the time interval $[0, 1]$ into K steps which we index them as q. In the initial state, $q = 0$, $\mathbf{\Omega}(0) = \mathbf{I}$, $\lambda_i(0) = \lambda_{N_i}$, and $\mathbf{v}_i(0) = \mathbf{v}_{N_i}$. In order to reduce the numerical error, we reinitialize the problem at the beginning of each step $q = 0, 1, \cdots, K$. Instead of aligning λ_{N_i} to λ_{M_i}, we align $\lambda_i(q)$ to λ_{M_i}. $\lambda_i(q)$ and $\mathbf{v}_i(q)$ are re-calculated with Equation 4 and current $\mathbf{\Omega}(q)$. The result $\dot{\mathbf{\Omega}}(q)$ can be used to calculate $\mathbf{\Omega}(q+1)$ as follows:

$$\mathbf{\Omega}(q+1) = \mathbf{\Omega}(q) + \frac{1}{K-q}\dot{\mathbf{\Omega}}(q). \tag{31}$$

After K steps, the desired $\mathbf{\Omega}(K)$ will be achieved and manifold M will be aligned to manifold N. The summary of the algorithm can be found in Algorithm 1.

Algorithm 1 Eigenvalue Alignment

Input: Closed 2D manifolds N and M, represented by triangle meshes, and constant k_1;
Output: Diagonal weight matrix $\mathbf{\Omega}(q)$ on N, aligning first k_1 nonzero eigenvalues from N to M;
Initialize $\mathbf{\Omega}(0) \leftarrow \mathbf{I}$, calculate matrices $\mathbf{W}$ and $\mathbf{S}$ on N, and $\lambda_{M_i}, \mathbf{v}_{M_i}, \lambda_{N_i}$, and $\mathbf{v}_{N_i}$, for $i = 1, 2, \ldots, k_1$;
while $q < K$ **do**
  Calculate $\lambda_i(q), \mathbf{v}_i(q)$, for $i = 1, 2, \ldots, k_1$ using Equation 4 with $\mathbf{\Omega}(q)$;
  Construct the quadratic programming problem using Equations 19, 25, and 27;
  Solve the quadratic programming problem to get $\dot{\mathbf{\Omega}}(q)$ and calculate $\mathbf{\Omega}(q+1)$;
  $q \leftarrow q + 1$;
end while

4 Experiments and Applications

The proposed algorithm and system are implemented using Python and C++ on a 64-bit Linux platform. The experiments are conducted on a computer with an Intel Core i7-3770 3.4 GHz CPU and 8 GB RAM. We apply our algorithm on 2D manifolds, represented with triangle meshes. In the experiments, we use hippocampi extracted from brain MR images and their surface meshes have around 5000 vertices. Besides the vertex number, there are two constants, K iteration and the first k_1 nonzero eigenvalues to be aligned. According to the algorithm described in Section 3, each iteration is an independent quadratic programming problem. Thus, the complexity is linear to the step number K. k_1 determines how many eigenvalues to be re-initialized at the beginning of each step. The algorithm calculates the eigenvalues by iterations with the complexity of $O(n^2)$ to the number of vertices and linear to k_1. The average computing time for around 5000 nodes, with $k_1 = 100$ and $K = 10$, is around 17 seconds. Note that, the larger the K is, the more accurate the approximation is, in terms of the linear interpolation. In practice, we found $K = 10$ is sufficient to get the accurate result with a reasonable computational time. Ideally, including more eigenvalues for alignment can be more accurate. However, the numeric eigenvalue calculation is not reliable on higher indexed eigenvalues, which will bring more unsuitability. It is noted that the unstable eigenfunctions are introduced by the symmetry. This is avoided by

applying some preprocessing with existing symmetry analysis algorithms. Our experiments show that the first 100 eigenfunctions carry sufficient geometry information and are also quite reliable. The middle range frequencies provide sufficient geometry information for the fine deformation. So we usually choose $k_1 = 100$ in our experiments. Details about how we choose K and k_1 in our experiments are provided in Section 4.1.1.

4.1 Experiments on Synthetic Data

4.1.1 Sensitivity Analysis

We analyze the sensitivity of our model with respect to the number of iteration (K) and eigenvalues (k_1). To this end, we employ the Bunny model with 3000 vertices and make a bump on the back of the bunny. Figure 1 shows the original and target bunnies. The dashed circle shows the bump made on the back of the bunny. We conduct an empirical study to map the original bunny to target one using 30, 50, and 80 eigenvalues and 10 iterations. The results are presented in Figure 2 and shown that by increasing the number of eigenvalues, the outcome is better to match the synthetic target results. We conduct another experiment and map the original bunny to the target one using 80 eigenvalues and 1, 5, and 10 iterations, respectively. Figure 3 shows the results of this mapping. As one can conclude, the outcome is improved from 1 iteration to 10 iterations.

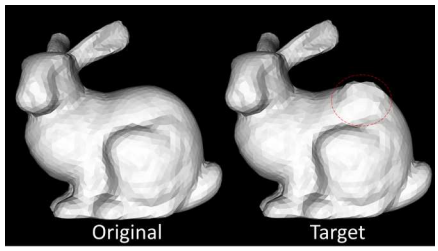

Fig. 1: We made a bump on the back of the bunny. The original and target bunnies are shown in this picture.

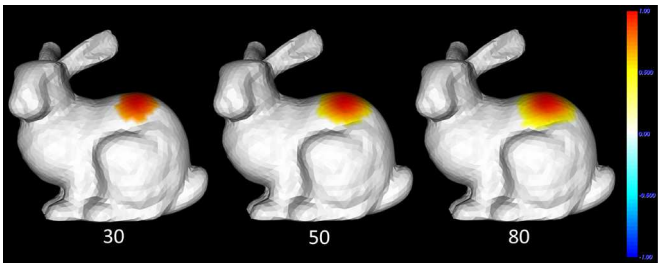

Fig. 2: The result of mapping the original bunny to the target one in Figure 1 using 30, 50, and 80 eigenvalues and 10 iterations.

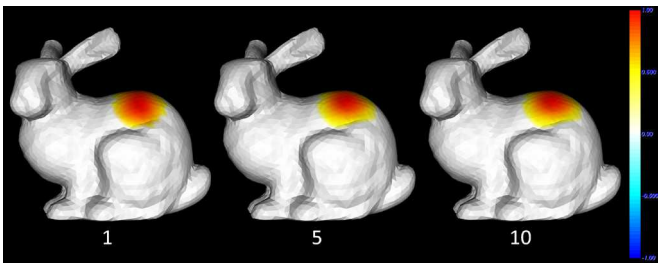

Fig. 3: The result of mapping the original bunny to the target one in Figure 1 using 80 eigenvalues and 1, 5, and 10 iterations.

4.1.2 Hippocampus Data

In order to evaluate the efficiency of our method, we synthetically generate some non-isometric deformations based on an initial shape. In this experiment, we use a hippocampus segmented from 3D brain MR images. The surface is then deformed manually to make a non-isometric deformation. Our spectrum alignment is applied on the first 100 nonzero eigenvalues. Note that, no correspondence information is used in the experiments.

In the first experiment, we synthetically generate a bump on the original surface. Then we align the original object to the bumped one to obtain the scale function. Figure 4a and 4b show the original and deformed objects, respectively. Figure 4c shows the result of mapping the original shape to the deformed one. The spectrum variation can detect and localize the non-isometric deformation clearly. The red color indicates the located dilating area. In order to see the values of scale function, we also provide the histogram in Figure 4d. The histogram has more positive areas than negative, which concludes to the shape expansion when mapping from the shape in Figure 4a to the one in Figure 4b. It is worthy to mention that we use a threshold to show the deformed area in Figure 4c. The threshold value ε is defined as follows:

$$\varepsilon = min(|min(\mathbf{\Omega})|, |max(\mathbf{\Omega})|). \tag{32}$$

area A_i which has scale values over the threshold ε indicates the expansion as shown in Figure 4c. When area A_i having scale values less than $-\varepsilon$, it indicates the shrinkage.

In the second experiment, we shrink one part of the original manifold. Then, we align the original shape to the shrunk one. Figure 5a and 5b shows the original and deformed shapes. Figure 5c shows the results of mapping. As can be seen, the local shrunk region is detected

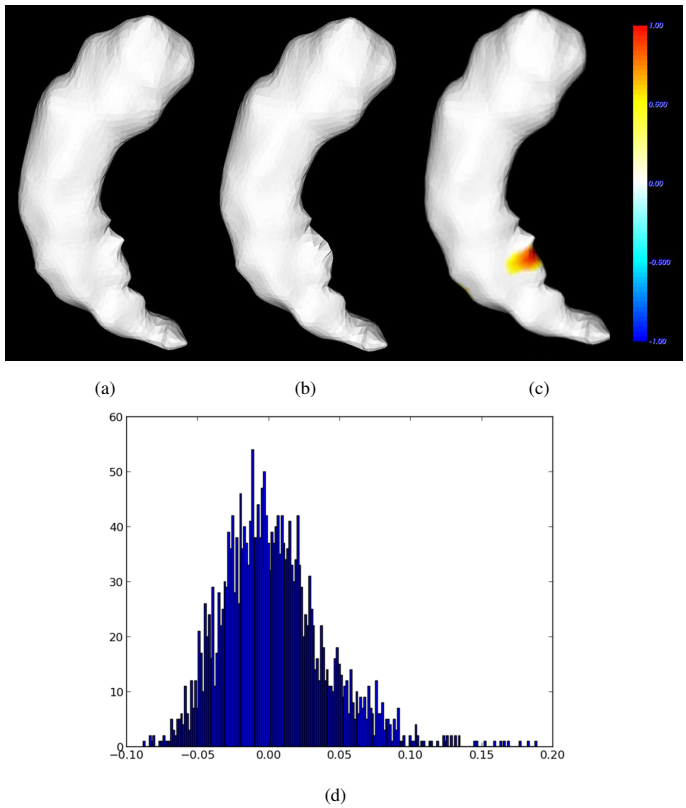

Fig. 4: The result of mapping the original 3D object to the synthetic one. (a) shows the original object. (b) is obtained by generating a bump on the original shape. (c) shows the result of mapping shape (a) to the one in (b) where the expansion is determined and located. The histogram of the scale matrix is presented in (d). The histogram has more positive area, which mean the shape has an expansion.

and pinpointed by our method. The blue color shows the contraction of the area. In order to see the distribution of the computed scale function, we present its histogram in 5d. The histogram has more negative areas, which concludes to the shape contraction when mapping from the shape in Figure 5a to the one in Figure 5b.

In the third experiment, we scale the manifold by a factor of 0.5 and align the original shape to the scaled one. Figure 6a shows the comparison of the original and scaled objects. Figure 6b shows the result of mapping the original shape to the scaled one. As can be seen the whole surface is blue which means it is globally shrunk. The histogram result from this mapping is shown in Figure 6c. The center of the histogram is moved to -0.661 (equal to the changes of the Voronoi areas of the two shapes) which shows the shrinkage of the whole object while there exist almost no local spectral variations across different vertices.

These experiments clearly demonstrate that our method is able to detect and localize non-isometric deformations as well as global deformations.

4.2 Applications on Real Patient Imaging Data

To evaluate our method on real imaging data, we have conducted two studies: Epilepsy study and Alzheimer study. In both studies, hippocampus, which is located in temporal lobe of brain, is affected by these diseases.

4.2.1 Epilepsy Study and Diagnosis

Mesial temporal lobe epilepsy (mTLE) is one of the most common types of focal epilepsy. Among mTLE structural abnormalities, hippocampus is one of the most frequent structures that can be affected. As indicated in [11], epilepsy may cause shrinkage of the affected hippocampus in comparison to the non-affected one. Note that, traditional voxel-based approaches can determine expansion or shrinkage but cannot localize deformations. We apply our method on twenty TLE patients for localizing and quantifying the shape variation between left and right hippocampi. In our data, half number of the patients are reported to have left defected hippocampus and the other half have abnormality in the right hippocampus. To generate the 3D hippocampus surface, right and left hippocampi are segmented manually using MRIcro Tool from 3D T1 images. Right hippocampi are then mirrored in order to have the same orientation as the left ones. For epilepsy study, we have also applied our spectrum alignment to the first 100 nonzero eigenvalues in order to obtain the scale function.

The abnormal deformations are accurately localized and quantified, which are consistent with clinical findings in the patients' medical records. In Figure 7, column 1 and 2 show samples of left and right hippocampi. Column 3 shows the computed scale function distributions on the left hippocampus surface when mapping from the left one to the right. The colors denote the values of scale function in each vertices. Red means dilating, blue means contraction, and white means no distortion. According to the clinical record, Figure 7a is for a patient case that has left abnormal hippocampus, therefore, mapping from the left hippocampus to the right displays more expansion (indicated in red), i.e., the left hippocampus is shrunk (diseased) compared to the right, normal one. Figure 7b depicts another patient case that has the

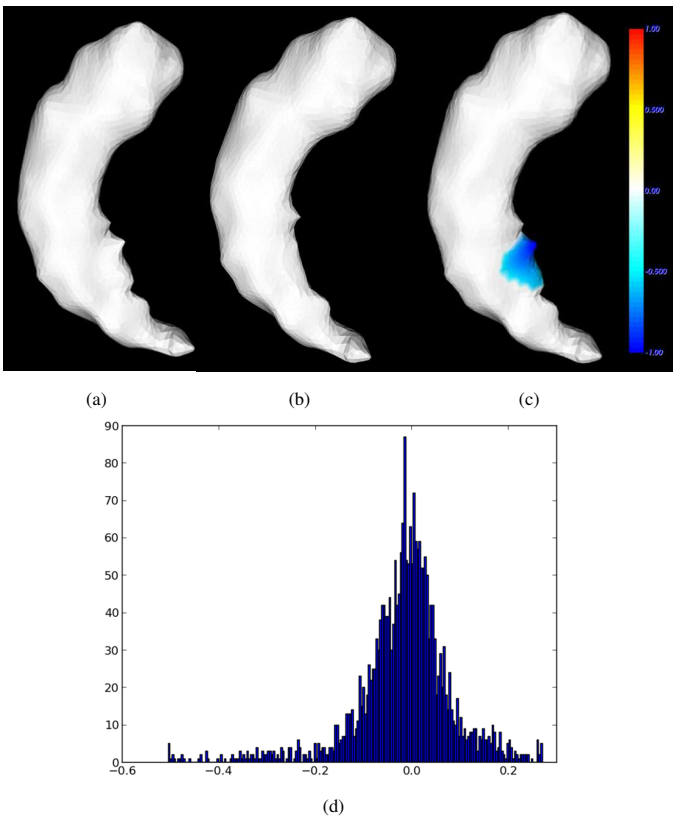

Fig. 5: The result of mapping the original 3D object to a modified object generated by shrinking a local area of the original data. (a) shows the original object. (b) shows the modified object generated by shrinking a local part of the original shape. (c) shows the result of mapping the original shape in (a) to the shrunk shape in (b), where shrinkage is localized. The histogram of the computed scale function is presented in (d). The histogram has more negative area, which means the shrinkage of the shape.

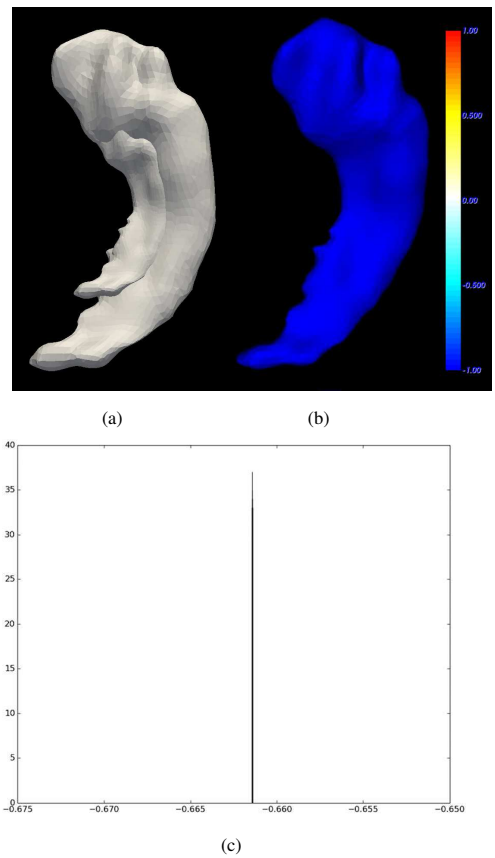

Fig. 6: The result of mapping the original 3D object to the object which generated by scaling the original data by a factor of 0.5. (a) shows the original object in comparison to the synthetically scaled one. (b) shows the result from mapping the original shape to the scaled one. The whole object surface is blue which means the object is globally shrunk. The histogram of the scale matrix is presented in (c). The histogram center has moved to -0.661 with very little eigenvalue variations across vertices.

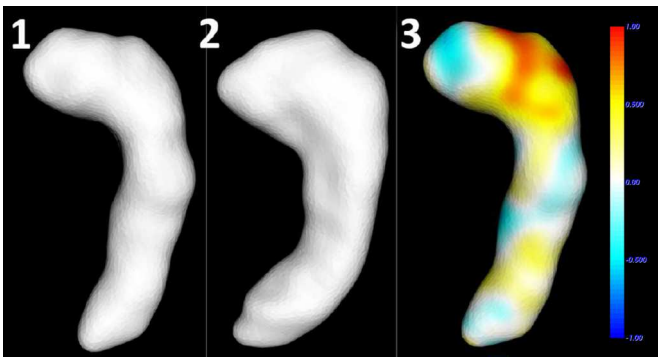

(a)

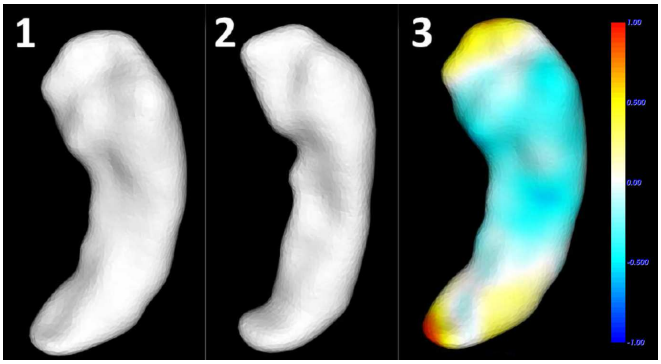

(b)

Fig. 7: The results of mapping the left hippocampus to right one for two cases. (a) shows a case in which the left hippocampus is affected by epilepsy. (b) shows a case that has right abnormal hippocampus. The first, second, and third columns represent left hippocampus, right hippocampus, and the result of mapping left hippocampus to right one, respectively.

right defected hippocampus. When mapping from the left hippocampus to the right, the scale distribution displayed on the left hippocampus surface mainly shows the shrinkage (indicated in blue) which indicates the right hippocampus is shrunk (diseased) in comparison to the left hippocampus.

To check how the eigenfunctions vary after changing the eigenvalues, we select the 12th eigenvalue and show the eigenfunctions corresponding to this eigenvalue on the source manifold before and after mapping to the target manifold. Figure 8 shows the 12th eigenfunction of the original left hippocampus (first column), the original right hippocampus (second column), and the spectrum-aligned left hippocampus (third column). The eigenfunctions are normalized between -1 and 1. The values of eigenfunction at each vertex are expressed with color map, where red means larger value, blue means smaller ones, and white means zero. Comparing the eigenfunction patterns before and after the alignment, a great improvement is obtained and the pattern of the eigenfunction in the source manifold has changed in order to well align to the target manifold.

In order to show the variation of eigenvalues of the manifolds before and after alignment, we list the 2nd to 8th eigenvalues of left hippocampus (before and after mapping) and right hippocampus in Table 1. The eigenvalues are normalized by the first nonzero one to remove the scale factor. It can be seen that after applying the spectrum alignment algorithm, the eigenvalues of the source manifold have changed to well align with the target ones.

4.2.2 Alzheimer Study and Diagnosis

Alzheimer disease (AD) is a brain mis-functionality that is caused by the loss of neurons and neural volume. Hippocampus, a part of the mesial temporal lobe memory system, is vulnerable to damage in the

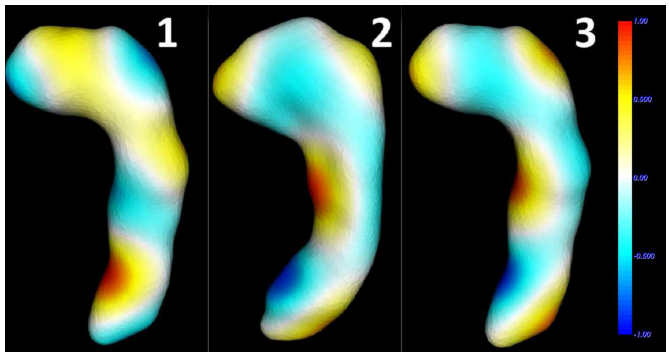

Fig. 8: The 12th eigenfunction of the original left hippocampus (first column), the original right hippocampus (second column), and the spectrum-aligned left hippocampus (third column). The pattern of the eigenfunction for the left hippocampus shape has been changed in order to map the right one.

Table 1: The result of aligning eigenvalues from the left hippocampus to right one using the same case as in Figure 7a.

Manifold	$\lambda_i/\lambda_1, i \in [2, 8]$
Left Hippocampus	3.87, 7.76, 11.93, 14.22, 15.88, 18.49, 20.62
Right Hippocampus	4.36, 7.75, 11.20, 12.62, 16.60, 18.35, 21.73
Aligned Left One	4.36, 7.75, 11.19, 12.62 , 16.59, 18.34, 21.73

early stage of Alzheimer. Volumetric longitudinal studies [40, 37] using MR images show hippocampal atrophy during time in comparison to healthy cases. In many clinical studies, it was observed that the variation is more in the left hippocampus than the right one and there exists a deformation of CA1 region in hippocampus which can be extended to the subiculum region [19]. In this paper, we conduct experiments on the dataset provided by the Alzheimer's Disease Neuroimaging Initiative (ADNI) to show that our shape variation analysis method confirms the aforementioned observation.

We employ ten healthy and ten AD cases aging between 74-80 which have longitudinal study for one year to track and compare the deformation of left and right hippocampi. Our motivating data example consists of ten healthy and ten AD patients which were downloaded from the hippocampal study in ADNI and were segmented using Freesurfer software [4]. The 3D object and surface meshes are generated using the method mentioned before and the scale function is obtained by applying our proposed method. According to our results, the AD patients' left and right hippocampi are shrunk after one year. The average of shrinkage for AD cases is more than health cases in both right and left hippocampi. We also confirm that in AD patients the average of shrinkage is more in the left hippocampus than right one. In addition to the global deformation, the local analysis using our method shows that the middle region of hippocampus, called CA1, is affected more severely in both left and right hippocampi. Figure 9 shows the results of applying the proposed method on an AD and healthy cases for left and right hippocampi. The baseline hippocampus is aligned to the hippocampus after one year and the results are shown on the source manifold. As one can see, the left and right hippocampi in AD cases have shrinkage in the middle of the hippocampus. This can be extend to the tail of hippocampus in some cases. Also Figure 9 shows that in the normal case the hippocampus has little change after one year. Therefore, our results confirm the clinical observation.

4.3 Comparisons to Spatial Registration Methods

In order to further demonstrate the capabilities of our method, we compare the results of our algorithm with the ones employing non-rigid Iterative Closest Point (ICP) algorithm [1]. In the non-rigid ICP method, we fist find the rigid transformation of the source manifold to the tar-

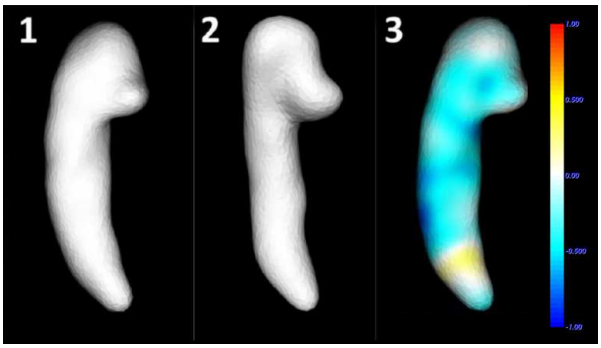

(a)

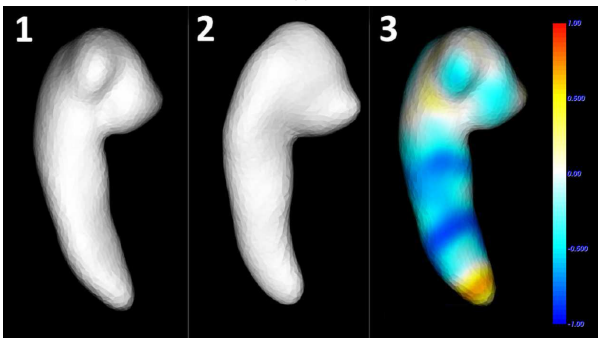

(b)

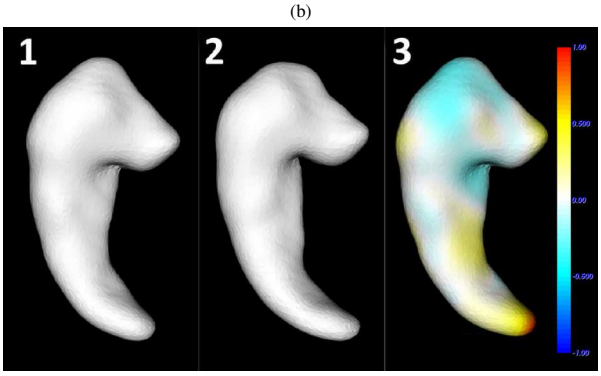

(c)

Fig. 9: Longitudinal study for Alzheimer disease. Column 1 shows the baseline hippocampus and column 2 shows the hippocampus after 1 year. Column 3 shows the deformation (scale function) results from aligning the baseline hippocampus to the one after one year. (a) and (b) show the left and right hippocampi results for an AD patient, respectively. (c) shows the result for a hippocampus in a normal case.

get. Then, using the non-rigid registration method, we further register the manifold to the target to build the point-to-point correspondence. The displacement of each corresponding point pairs between the rigid registered source manifold and the target manifold presents the deformation distribution. In order to compare two methods, we synthetically deform a shape by stretching and bending the geometry from both top and bottom sides of the shape as shown in Figure 10. Column 1 and 2 show the original and the synthetically deformed shapes, respectively. Figure 10a and 10b show different views of the shapes. Column 3 and 4 show the results of spectrum alignment and non-rigid ICP methods, respectively. From the results, we can see that our method detects the expansions on both ends while the non-rigid ICP method detects the shape deformation at the bottom end instead of both ends.

In order to further compare two methods, we also make an expansion in one part of the synthetically deformed shape as in Figure 10 and compare the results. Figure 11 shows the original and synthetically deformed shapes in column 1 and 2, respectively. The locally deformed area is marked with a red circle. The results of the spectrum alignment and non-rigid ICP registration method are shown in column 3 and 4. As we can see, our spectrum alignment method detects the deformation more accurately than the non-rigid ICP method. The local expansions, including previously deformed ends in Figure 10, are exactly localized.

Our method can also detect the deformation of the shapes using different number of eigenvalues. This allows us to analyze shape deformation using lower or higher frequency bands. Figure 12 shows the results of spectrum alignment of a shape in 12a to one in 12b using different sets of eigenvalues. As we can see, subtle deformations will be added to the results when using higher indexed number of eigenvalues.

The qualitative and quantitative comparisons of our method, non-rigid ICP method and voxel-based method are documented in Table 2. The voxel-based method is based on the number of the voxels in the original 3D MR images [11]. Using this method only the global volume of the hippocampus can be detected and the running time for this method is more than 45 seconds. Based on our experiments, the computing time for our method is less than 20 seconds while ICP method costs over 60 seconds. In order to quantitatively evaluate the capabilities of these methods in localizing deformations, we use the following metric to compute their agreement, A, as follows:

$$A = \frac{D \cap G}{D \cup G}, \tag{33}$$

where D is the localized deformation region and G is the known ground truth of the deformed region. The experiments demonstrate that the average outcome for our method is about 92%; for ICP method is about 81%; and for voxel-based method is about 85%. Therefore, our method outperforms the non-rigid ICP method in these shapes with few landmarks and features. Our method performs much better when there is mixture of different types of deformations.

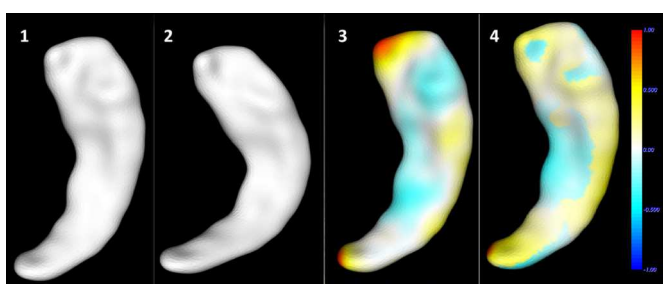

(a)

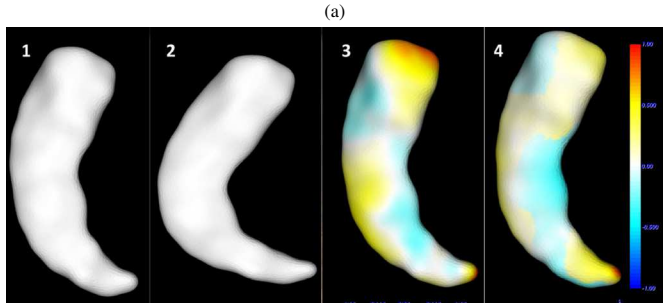

(b)

Fig. 10: The results of mapping the original shape to the synthetically deformed shape using our method and non-rigid ICP. Column 1 shows the original shape. Column 2 shows the synthetic data which is bent and stretched at both ends. Column 3 and 4 show the results of mapping the shape in column 1 to column 2 using our method and non-rigid ICP technique, respectively. (a) and (b) show the different views of the shape.

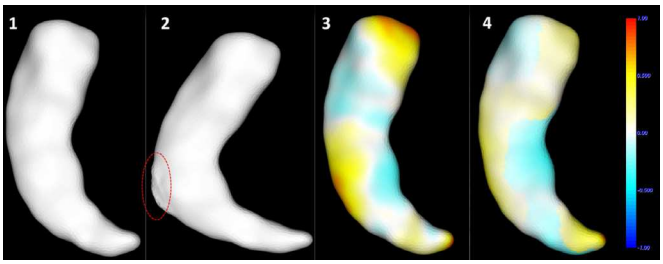

(a)

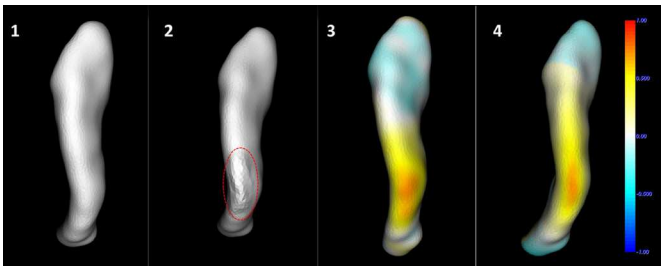

(b)

Fig. 11: We manually add an expansion to the deformed shape in Figure 10 to compare our spectrum alignment method and the non-rigid ICP results. The locally deformed area is marked with a red circle. Column 1 shows the original shape. Column 2 shows the locally expanded shape from Figure 10 (Column 2). Column 3 and 4 shows the results of aligning column 1 to column 2 using our method and the non-rigid ICP technique, respectively. (a) and (b) show different views of the shapes.

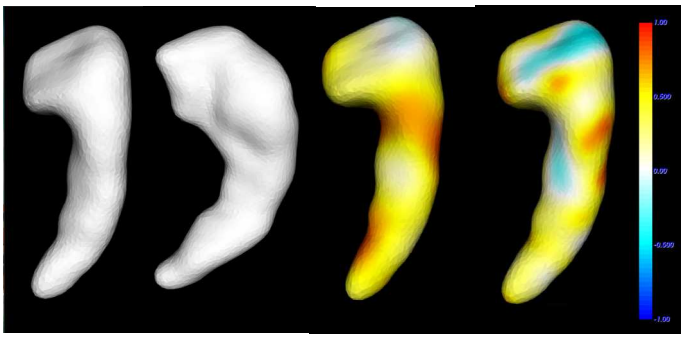

(a) (b) (c) (d)

Fig. 12: The results of spectrum alignment of a shape in (a) to one in (b) using different sets of eigenvalues. (c) and (d) show the results of using first 20 and 80 eigenvalues.

Table 2: Comparison among our method, non-rigid ICP and voxel-based method.

Capabilities	Our Method	Non-rigid ICP	Voxel-based
Registration-Free	✓		
Global Deformation	✓	✓	✓
Local Deformation	✓	✓	
Multi-scale Deformation Quantification	✓		
Average accuracy: A	92%	81%	85%
Computation	$\approx$ 20s	$>$ 60s	$>$ 45s

5 Conclusion and Discussion

In this paper, we have introduced a new method based on our developed spectrum variation theorems for localizing and quantifying deformations between surface shapes. We have proved that the eigenvalues of the spectrum constitute an analytic function of a scale function defined on the Riemann metric. The deformation is an integral of the derivative of the scale function. The theorem applies both continuous analytic and discrete cases, therefore, warrants an algorithm to align the shape spectra of discrete shapes represented with triangle meshes. Given two closed triangle meshes, the spectra can be aligned from one to another with a scale function defined on each vertex. Our extensive experiment results have demonstrated that the proposed method can detect the global and local deformation of shapes. Our applications to real epilepsy and Alzheimer data have shown its potential in clinical diagnosis. Furthermore, the comparisons to non-rigid ICP method and voxel-based method have indicated that our method has more advantages.

There are some limitations for our method. The proposed method can be applied to map two shapes in the same class, but is not suitable to address the deformations between two objects in different classes. Another limitation for this method is regarding symmetric shapes like cubic, sphere, etc. The alignment of eigenvalues of the Laplace Beltrami matrices for these shapes is unstable to achieve. Therefore, our method in the current form cannot be applied to these kinds of shapes. We plan to improve our method along these two directions in the future.

Acknowledgments

The authors wish to thank Dr. Hamid Soltanian-Zadeh from Department of Radiology at Henry Ford Health System for providing the data for some of the experiments and Dr. Farshad Fotouhi for his valuable input. The research is supported in part by grants NSF CNS-1647200, IIS-0915933, IIS-0937586 and ZJNSF LZ16F020002.

References

[1] P. Besl and N. McKay. A method for registration of 3-D shapes. *IEEE Trans. on Pattern Analysis and Machine Intelligence*, 14(2):239–256, 1992.

[2] A. Bronstein, M. Bronstein, and R. Kimmel. Generalized multidimensional scaling: a framework for isometry-invariant partial surface matching. *Proc Natl Acad Sci U S A.*, 103(5):1168–1172, 2006.

[3] J. J. Caban, P. Rheingans, and T. Yoo. An evaluation of visualization techniques to illustrate statistical deformation models. *Computer Graphics Forum*, 30(3):821–830, 2011.

[4] A. Dale, B. Fischl, and M. Sereno. Cortical surface-based analysis. i. segmentation and surface reconstruction. *Neuroimage*, 9(2):179–194, 1999.

[5] M. El-Mehalawi and R. Miller. A database system of mechanical components based on geometric and topological similarity. part i: Representation. *Computer-Aided Design*, 35:83–94, 2003.

[6] M. El-Mehalawi and R. Miller. A database system of mechanical components based on geometric and topological similarity. part ii: Indexing, retrieval, matching, and similarity assessment. *Computer-Aided Design*, 35:95–105, 2003.

[7] J. Fiot, H. Raguet, L. Risser, L. Cohen, J. Fripp, and F. Vialard. Longitudinal deformation models, spatial regularizations and learning strategies to quantify alzheimer's disease progression. *NeuroImage*, 4:718–729, 2014.

[8] J. Han, P. Yin, Y. He, and F. Gu. Enhanced ICP for the registration of large-scale 3D environment models: An experimental study. *Sensors*, 16(2), 2016.

[9] M. Hermann, A. C. Schunke, T. Schultz, and R. Klein. A visual analytics approach to study anatomic covariation. In *Proc. IEEE PacificVis*, pp. 161–168, 2014.

[10] M. Hermann, A. C. Schunke, T. Schultz, and R. Klein. Accurate interactive visualization of large deformations and variability in biomedical image ensembles. *IEEE Trans. on Visualization and Computer Graphics*, 22(1):708–717, 2016.

[11] K. Jafari-Khouzania, K. Elisevichb, S. Patela, B. Smithc, and H. Soltanian-Zadeh. Flair signal and texture analysis for lateralizing mesial temporal lobe epilepsy. *NeuroImage*, 49(2):1159–1571, 2010.

[12] V. Jain and H. Zhangu. Robust 3D shape correspondence in the spectral domain. In *IEEE International Conference on Shape Modeling and Applications*, p. 19, 2006.
[13] M. Jenkinson and S. Smith. A global optimisation method for robust affine registration of brain images. *Medical Image Analysis*, 5(2):143–156, 2001.
[14] Z. Karni and C. Gotsman. Compression of soft-body animation sequences. *Computers and Graphics*, 28(1):25–34, 2004.
[15] A. Kovnatsky, M. M. Bronstein, X. Bresson, and P. Vandergheynst. Functional correspondence by matrix completion. In *Proc. IEEE Conf. on Computer Vision and Pattern Recognition (CVPR)*, pp. 905–914, 2015.
[16] A. Kovnatsky, M. M. Bronstein, A. M. Bronstein, K. Glashoff, and R. Kimmel. Coupled quasi-harmonic bases. *Computer Graphics Forum*, 32(2):439–448, 2013.
[17] B. Lévy. Laplace-beltrami eigenfunctions: Towards an algorithm that understands geometry. In *IEEE International Conference on Shape Modeling and Applications, invited talk*, 2006.
[18] N. Li, S. Wang, M. Zhong, Z. Su, and H. Qin. Generalized local-to-global shape feature detection based on graph wavelets. *IEEE Trans. on Visualization and Computer Graphics*, 11(6):1–14, 2015.
[19] S. Li, F. Shi, F. Pu, X. Li, T. Jiang, S. Xie, and Y. Wang. Hippocampal shape analysis of alzheimer disease based on machine learning methods. *AJNR Am J Neuroradiol*, 28(7):1339–1345, 2007.
[20] M. Miller, J. Ratnanather, D. Tward, T. Brown, D. Lee, M. Ketcha, K. Mori, M. Wang, S. Mori, M. Albert, L. Younes, and B. R. Team. Network neurodegeneration in alzheimers disease via mri based shape diffeomorphometry and high-field atlasing. *Frontiers in Bioengineering and Biotechnology*, 3, 2015.
[21] R. Osada, T. Funkhouser, B. Chazelle, and D. Dobkin. Shape distributions. *ACM Trans. on Graphics*, 21(4):807–832, 2002.
[22] M. Ovsjanikov, M. Ben-Chen, F. Chazal, and L. Guibas. Analysis and visualization of maps between shapes. *Computer Graphics Forum*, 32(6):135–145, 2013.
[23] M. Ovsjanikov, M. Ben-Chen, J. Solomon, A. Butscher, and L. Guibas. Functional maps: A flexible representation of maps between shapes. *ACM Trans. Graphics*, 31(4):30:1–30:11, 2012.
[24] N. Peinecke, F.-E. Wolter, and M. Reuter. Laplace spectra as fingerprints for image recognition. *Computer-Aided Design*, 39(6):460–476, 2007. doi: 10.1016/j.cad.2007.01.014
[25] M. Reuter. Hierarchical shape segmentation and registration via topological features of laplace-beltrami eigenfunctions. *International Journal of Computer Vision*, 89(2):287–308, 2010.
[26] M. Reuter, M. Niethammer, F. Wolter, S. Bouix, and M. Shenton. Global medical shape analysis using the volumetric laplace spectrum. In *International Conference on Cyber worlds, NASA-GEM Workshop*, pp. 417–426, 2007.
[27] M. Reuter, F. Wolter, and N. Peinecke. Laplace-beltrami spectra as "Shape-DNA" of surfaces and solids. *Computer-Aided Design*, 38(4):342–366, 2006.
[28] M. Reuter, F. Wolter, M. Shenton, and M. Niethammer. Laplace beltrami eigenvalues and topological features of eigenfunctions for statistical shape analysis. *Computer-Aided Design*, 41(10):739–755, 2009.
[29] E. Rodolà, L. Cosmo, M. M. Bronstein, A. Torsello, and D. Cremers. Partial functional correspondence. *Computer Graphics Forum*, 2016. doi: 10.1111/cgf.12797
[30] E. Rodolà, A. Torsello, T. Harada, Y. Kuniyoshi, and D. Cremers. Elastic net constraints for shape matching. In *IEEE International Conference on Computer Vision*, pp. 1169–1176, 2013.
[31] R. M. Rustamov. Laplace-beltrami eigenfunctions for deformation invariant shape representation. In *Fifth Eurographics symposium on Geometry processing*, pp. 225–233, 2007.
[32] R. M. Rustamov, M. Ovsjanikov, O. Azencot, M. Ben-Chen, F. Chazal, and L. Guibas. Map-based exploration of intrinsic shape differences and variability. *ACM Trans. Graphics*, 32(4):72:1–72:12, 2013.
[33] Y. Shi, R. Lai, R. Gill, D. Pelletier, D. Mohr, N. Sicotte, and A. Toga. Conformal metric optimization on surface (cmos) for deformation and mapping in laplace-beltrami embedding space. In *14th International Conference on Medical Image Computing and Computer-assisted Intervention - Volume Part II*, pp. 327–334, 2011.
[34] Y. Shi, R. Lai, D. J. J. Wang, D. Pelletier, D. Mohr, N. Sicotte, and A. W. Toga. Metric optimization for surface analysis in the laplace-beltrami embedding space. *IEEE Trans. on medical imaging*, 33(7):1447–1463, 2014.
[35] A. Sotiras, C. Davatzikos, and N. Paragios. Deformable medical image registration: A survey. *IEEE Trans Med Imaging*, 32(7):1153–1190, 2013.
[36] D. Tsuzukia, H. Watanabec, I. Danb, and G. Taga. Minr 10/20 system: Quantitative and reproducible cranial landmark setting method for mri based on minimum initial reference points. *Neuroscience Methods*, In Press, 2016.
[37] L. Wang, A. M. Fagan, A. R. Shah, M. F. Beg, J. G. Csernansky, J. C. Morris, and D. M. Holtzman. Csf proteins predict longitudinal hippocampal degeneration in early stage dementia of the alzheimer type. *Alzheimer Dis Assoc Disord*, 26(4):314–321, 2012.
[38] T. Windheuser, U. Schlickewei, F. R. Schmidt, and D. Cremers. Large-scale integer linear programming for orientation preserving 3d shape matching. *Computer Graphics Forum*, 30(5):1471–1480, 2011.
[39] H. Wolfson and I. Rigoutsos. Geometric hashing: an overview. *IEEE Computing in Science and Engineering*, 4:10–21, 1997.
[40] C. Zarow, L. Wang, H. Chui, M. Weiner, and J. Csernansky. Mri shows more severe hippocampal atrophy and shape deformation in hippocampal sclerosis than in alzheimer's disease. *International Journal of Alzheimer's Disease*, Volume 2011(483972), 2011.
[41] W. Zeng, L. M. Lui, L. Shi, D. Wang, W. C. Chu, J. C. Cheng, J. Hua, S.-T. Yau, and X. Gu. Shape analysis of vestibular systems in adolescent idiopathic scoliosis using geodesic spectra. In *Proceedings of the 13th International Conference on Medical Image Computing and Computer Assisted Intervention*, pp. 538–546, 2010.
[42] K. Zhou, J. Synder, B. Guo, and H. Shum. Iso-charts: Stretch-driven mesh parameterization using spectral analysis. In *Eurographics/ACM SIGGRAPH Symposium on Geometry Processing*, pp. 45–54, 2004.
[43] G. Zou, J. Hu, X. Gu, and J. Hua. Authalic parameterization of general surfaces using lie advection. *IEEE Transactions on Visualization and Computer Graphics*, 17(12):2005–2014, 2011.
[44] G. Zou, J. Hua, Z. Lai, X. Gu, and M. Dong. Intrinsic geometric scale space by shape diffusion. *IEEE Transactions on Visualization and Computer Graphics*, 15(6):1193–1200, 2009.

A Proof of Theorem 1

Proof. ω is a nonnegative and continuously differentiable function, and Δ^g is analytic. We can compute the derivative of the eigenvalue in Equation 6, and get

$$\Delta^g \dot{f}_i = -\dot{\lambda}_i \omega f_i - \lambda_i \dot{\omega} f_i - \lambda_i \omega \dot{f}_i.$$

Then, we multiply both sides with f_i and take the integral on M to get

$$\int_M f_i \Delta^g \dot{f}_i d\sigma = -\dot{\lambda}_i \int_M \omega {f_i}^2 d\sigma - \lambda_i \int_M \dot{\omega} {f_i}^2 d\sigma - \int_M \dot{f}_i \lambda_i \omega f_i d\sigma,$$

which can be simplified, based on Equations 6 and 7, as

$$\int_M f_i \Delta^g \dot{f}_i d\sigma = -\dot{\lambda}_i - \lambda_i \int_M \dot{\omega} {f_i}^2 d\sigma + \int_M \dot{f}_i \Delta^g f_i d\sigma.$$

Note that, M is a closed manifold. According to divergence theorem, we can have

$$\int_M f_i \Delta^g \dot{f}_i d\sigma = -\int_M \nabla \dot{f}_i \cdot \nabla f_i d\sigma = \int_M \dot{f}_i \Delta^g f_i d\sigma,$$

hence we get Equation 9. □

B Proof of Theorem 2

Proof. We can compute the derivative of the eigenvalue equation, Equation 10, and get

$$\mathbf{W}\dot{\mathbf{v}}_i = \dot{\lambda}_i \mathbf{\Omega S} \mathbf{v}_i + \lambda_i \dot{\mathbf{\Omega}} \mathbf{S} \mathbf{v}_i + \lambda_i \mathbf{\Omega S} \dot{\mathbf{v}}_i,$$

multiply $\mathbf{v}_i^T$ from the left to obtain

$$\mathbf{v}_i^T \mathbf{W} \dot{\mathbf{v}}_i = \dot{\lambda}_i \mathbf{v}_i^T \mathbf{\Omega S} \mathbf{v}_i + \lambda_i \mathbf{v}_i^T \dot{\mathbf{\Omega}} \mathbf{S} \mathbf{v}_i + \mathbf{v}_i^T \lambda_i \mathbf{\Omega S} \dot{\mathbf{v}}_i,$$

and simplify it, based on Equations 10 and 11, as

$$\mathbf{v}_i^T \mathbf{W} \dot{\mathbf{v}}_i = \dot{\lambda}_i + \lambda_i {\mathbf{v}_i}^T \dot{\mathbf{\Omega}} \mathbf{S} \mathbf{v}_i + {\mathbf{v}_i}^T \mathbf{W}^T \dot{\mathbf{v}}_i.$$

Finally, we obtain Equation 13 as $\mathbf{W}$ is symmetric. □